Direct multi-dimensional Chebyshev polynomial based reconstruction for Magnetic Particle Imaging

Christine Droigk, Marco Maass, and Alfred Mertins

Institute for Signal Processing, University of Lübeck, Lübeck, Germany

E-mail: c.droigk@uni-luebeck.de, marco.maass@uni-luebeck.de, alfred.mertins@uni-luebeck.de

December 2021

Abstract. Magnetic Particle Imaging is a tomographic imaging technique that measures the voltage induced due to magnetization changes of magnetic nanoparticle distributions. The relationship between the received signal and the distribution of the nanoparticels is described by the system function. A common method for image reconstruction is using a measured system function to create a system matrix and set up a regularized linear system of equations. Since the measurement of the system matrix is time-consuming, different methods for acceleration have been proposed. These include modeling the system matrix or using a direct reconstruction method in time, known as X-space reconstruction. In this work, based on the simplified Langevin model of paramagnetism and certain approximations, a direct reconstruction technique for Magnetic Particle Imaging in the frequency domain with two- and three-dimensional Lissajous trajectory excitation is presented. The approach uses Chebyshev polynomials of second kind. During reconstruction, they are weighted with the frequency components of the voltage signal and additional factors and then summed up. To obtain the final nanoparticle distribution, this result is rescaled and deconvolved. It is shown that the approach works for both simulated data and real measurements. The obtained image quality is comparable to a modeled system matrix approach using the same simplified physical assumptions and no relaxation effects. The reconstruction of a $31 \times 31 \times 31$ volume takes less than a second and is up to 25 times faster than the state-of-the-art Kaczmarz reconstruction. Besides, the derivation of the proposed method shows some new theoretical aspects of the system function and its well-known observed similarity to tensor products of Chebyshev polynomials of second kind.

1. Introduction

Magnetic Particle Imaging (MPI) is a tracer based medical imaging technology which was introduced by Gleich and Weizenecker [1]. It captures the spatial distribution of superparamagnetic iron oxide nanoparticles (SPIOs). This is commonly done by generating certain magnetic fields which lead to a field-free point (FFP) that moves inside an area of interest on a given periodic trajectory. A common choice is a Lissajous trajectory. The SPIOs change their magnetization and induce a voltage

signal in the receive coils. The main contribution comes from the SPIOs in the region of the FFP. The relationship between the received voltage signal and the SPIO distribution is described by the so-called system function which in the discrete setting is represented by the system matrix. Neglecting certain particle interactions, the MPI signal can be seen as the integral over the product of system function and SPIO concentration. A typical method for image reconstruction is the use of a measured system matrix [1]. For this, a delta sample of SPIOs is moved by a robot to all spatial points of interest inside the field of view (FOV) and the corresponding signals are measured. Dependent on the resolution, size, and dimension, this procedure can take up to several days [2]. With the measured system matrix and the received voltage signal, a system of linear equations is set up. Since the linear system is usually ill-posed [3–5], it is regularized and then solved by using iterative methods like the Kaczmarz algorithm [6]. In general, the entire procedure has certain drawbacks like the long system matrix acquisition time and noise in the measurements. As an alternative, modeling of the system matrix by describing the physical processes has been proposed, which is a challenging task. For one-dimensional excitation patterns that assume infinitely fast relaxation of the SPIOs, a simplified equilibrium model was proposed in [7]. More involved models that incorporate the Brownian rotation or Neel rotation [8] were presented for one-dimensional excitation patterns [9] and for 2D Lissajous type excitation patterns [10]. Relying on the equilibrium model and the Langevin model of paramagnetism, direct reconstruction methods in time-signal domain were successfully performed for one-dimensional excitation including 2D and 3D Cartesian like sampling patterns, commonly known under the name X-space reconstruction [11, 12]. Besides, a direct reconstruction for one-dimensional excitation in the temporal Fourier domain was proposed using Chebyshev polynomials [7]. Later, both reconstructions were shown to be equivalent [13]. In [14], the X-space approach was extended to non-Cartesian FFP trajectories. In addition, there exist other model based reconstruction techniques for the two-dimensional case which use a simulated system matrix instead of a measured one [15]. However, this procedure is not a direct method and still relies on solving the inverse problem by inverting the system matrix. Another approach uses the Chebyshev transformation to compress a measured system matrix. A compression to only one value per row allows for a direct inversion [16], but this approach still needs a system matrix.

In this work, we propose a direct reconstruction technique for two- and three-dimensional Lissajous-type excitation patterns for MPI. The reconstruction consists of the summation of Chebyshev polynomials of second kind weighted with the corresponding frequency components of the measured voltage signal and additional factors, followed by a deconvolution. It is derived from the recently published expression for the two- and three-dimensional system function by [17], which relies on the equilibrium model and has already given rise to a new reconstruction method with Bessel functions for one-dimensional excitation [18]. We show that the proposed direct reconstruction works for two- and three-dimensional simulated data as well as for the two-dimensional real measurements of the shape phantom and resolution phantom from

the OpenMPIData [19]. As expected, the image quality is not superior to state-of-the-art reconstruction with a measured system matrix, but comparable to model-based approaches that do not incorporate relaxation effects. Instead of a superior image quality, this method offers a very fast reconstruction even for 3D data and a fine grid. In contrast to [16] that also allows for a fast direct reconstruction, the proposed approach does not need a system matrix.

2. Methods

The system function $\boldsymbol{s} : \mathbb{R}^d \times \mathbb{R} \to \mathbb{R}^{n'}$ links the measured voltage signal $\boldsymbol{u} : \mathbb{R} \to \mathbb{R}^{n'}$ to the SPIO distribution $c : \mathbb{R}^d \to \mathbb{R}$. Here, d is the dimension of the SPIO distribution, and n' the number of receive coils. As the typical setting is to use $n' = d$ orthogonal receive coils, this is also assumed in the following. The relationship between received signal and SPIO distribution is denoted as [20]

$$\boldsymbol{u}(t) = \int_{\mathbb{R}^n} \boldsymbol{s}(\boldsymbol{x}, t) c(\boldsymbol{x}) \, \mathrm{d}\boldsymbol{x}. \tag{1}$$

The system function can be expressed as

$$s(\boldsymbol{x}, t) = -\mu_0 m \boldsymbol{P} \frac{\partial}{\partial t} \bar{\boldsymbol{m}}(\boldsymbol{x}, t) \tag{2}$$

with $\bar{\boldsymbol{m}} : \mathbb{R}^d \times \mathbb{R} \to \mathbb{R}^d$ being the mean magnetic moment of particles, μ_0 the vacuum permeability, m the magnetic moment of the nanoparticles, and $\boldsymbol{P}$ an $d \times d$ matrix denoting the homogeneous coil sensitivity profile. Following the equilibrium model that does not cover any relaxation effects, the mean magnetic moment is described by the Langevin function, leading to

$$s(\boldsymbol{x}, t) = \mu_0 m \boldsymbol{P} \frac{\partial}{\partial t} \boldsymbol{\mathscr{L}}(\beta \boldsymbol{G}(\boldsymbol{x}_{\mathrm{FFP}}(t) - \boldsymbol{x})) \tag{3}$$

where $\boldsymbol{G}$ is a $d \times d$ diagonal matrix containing the applied gradients of the selection field, β is a constant defined as $\beta = \frac{\mu_0 m}{k_B T}$ with the Boltzmann constant k_B, T is the temperature of the SPIOs, and $\boldsymbol{x}_{\mathrm{FFP}} : \mathbb{R} \to \mathbb{R}^d$ denotes the position of the FFP at time t depending on the excitation. The Langevin function itself reads

$$\mathscr{L}(x) = \begin{cases} \coth(x) - \frac{1}{x}, & x \in \mathbb{R} \backslash \{0\} \\ 0, & x = 0 \end{cases} \tag{4}$$

in 1D, and the n-dimensional extension of the Langevin function is defined as

$$\boldsymbol{\mathscr{L}}(\boldsymbol{x}) = \begin{cases} \mathscr{L}(\|\boldsymbol{x}\|) \frac{\boldsymbol{x}}{\|\boldsymbol{x}\|}, & \|\boldsymbol{x}\| \neq 0 \\ \boldsymbol{0}, & \|\boldsymbol{x}\| = 0, \end{cases} \tag{5}$$

where $\| \cdot \|$ denotes the Euclidean norm.

The proposed direct reconstruction method is derived from the representation of the two- and three-dimensional system function in Fourier space for the Langevin model and the use of Lissajous trajectories [17]. We will start to deal with the case of two-dimensional excitation and then extend the approach to 3D.

2.1. Two-dimensional Lissajous trajectory

We start with the case of two-dimensional excitation of a Lissajous-type with excitation frequencies $f_x = \frac{f_B}{N_B}$ and $f_y = \frac{f_B}{N_B - 1}$, where f_B is an arbitrary basis frequency and $N_B \in \mathbb{N}, N_B \geq 2$ a frequency divider. Then, the k-th frequency components $\boldsymbol{s}_k(\boldsymbol{x})$ of the temporal Fourier series of the system function $\boldsymbol{s}$ can be expressed as [17]

$$\begin{aligned}\boldsymbol{s}_k(\boldsymbol{x}) =& \operatorname{sgn}(\det(\boldsymbol{A}\boldsymbol{G}))\boldsymbol{C}_k \sum_{\lambda\in\mathbb{Z}} (-\mathrm{i})^\lambda \int_{\mathbb{R}^2} \left[\frac{\partial^2}{\partial z_1 \partial z_2} \mathscr{L}(\beta \boldsymbol{G}\boldsymbol{z})\right]_{\boldsymbol{z}=\boldsymbol{x}-\boldsymbol{u}} \\ & V_{-k+\lambda N_B}\left(\frac{G_x}{A_x}u_1\right) V_{k-\lambda(N_B-1)}\left(\frac{G_y}{A_y}u_2\right) \mathrm{d}\boldsymbol{u} \end{aligned} \tag{6}$$

with the matrix $\boldsymbol{C}_k$ given by

$$\boldsymbol{C}_k = -\frac{2k f_D \mathrm{i}}{\pi} \mu_0 m \boldsymbol{P}, \tag{7}$$

$\boldsymbol{A} = \operatorname{diag}(A_x, A_y)$ denoting the drive-field amplitudes in x- and y-direction, f_D denoting the frequency of the whole Lissajous trajectory, $\boldsymbol{G} = \operatorname{diag}(G_x, G_y)$, and z_1, z_2 and u_1, u_2 denoting the first and second component of $\boldsymbol{z}$ and $\boldsymbol{u}$, respectively. Besides,

$$V_n(x) = \begin{cases} \operatorname{rect}\left(\frac{x}{2}\right)\left(-\frac{U_{|n|-1}(x)\sqrt{1-x^2}}{|n|}\right), & n \neq 0 \\ \frac{\pi}{2}\operatorname{sgn}(x+1) - \operatorname{rect}\left(\frac{x}{2}\right)\arccos(x), & n = 0, \end{cases} \tag{8}$$

where U_n denotes the Chebyshev polynomial of second kind and n-th order.

The frequency components of the spatio-temporal Fourier series of the system function can be expressed as [17]

$$\begin{aligned}\hat{\boldsymbol{s}}_k(\boldsymbol{\omega}_x) =& \boldsymbol{C}_k \frac{\pi^2}{|\det \beta \boldsymbol{G}|} \sum_{\lambda\in\mathbb{Z}} (-1)^\lambda \hat{\mathscr{L}}\left(\frac{\boldsymbol{G}^{-1}\boldsymbol{\omega}_x}{\beta}\right) \\ & J_{-k+\lambda N_B}\left(\frac{A_x}{G_x}\omega_{x_1}\right) J_{k-\lambda(N_B-1)}\left(\frac{A_y}{G_y}\omega_{x_2}\right). \end{aligned} \tag{9}$$

Here, J_n is the n-th Bessel function of first kind. The spatial Fourier transform of the two-dimensional Langevin function is [17]

$$\hat{\mathscr{L}}(\boldsymbol{\omega}_x) = \frac{-\pi^2 \mathrm{i}\boldsymbol{\omega}_x}{\|\boldsymbol{\omega}_x\|} \int_0^\infty \cosh(t)\operatorname{csch}^2\left(\frac{\pi}{2}\|\boldsymbol{\omega}_x\|\cosh(t)\right) \mathrm{d}t. \tag{10}$$

In [21], it was already mentioned that only one or two summands contribute significantly to the infinite sum in (6) and (9). This is due to the limited overlap in the product of the Fourier transformed Langevin function with the tensor product of the Bessel functions. In Fig. 1, the corresponding functions are plotted.

The Fourier transformed Langevin function is exponentially decreasing in an isotropic way. The Bessel functions oscillate, and it can be observed that the position

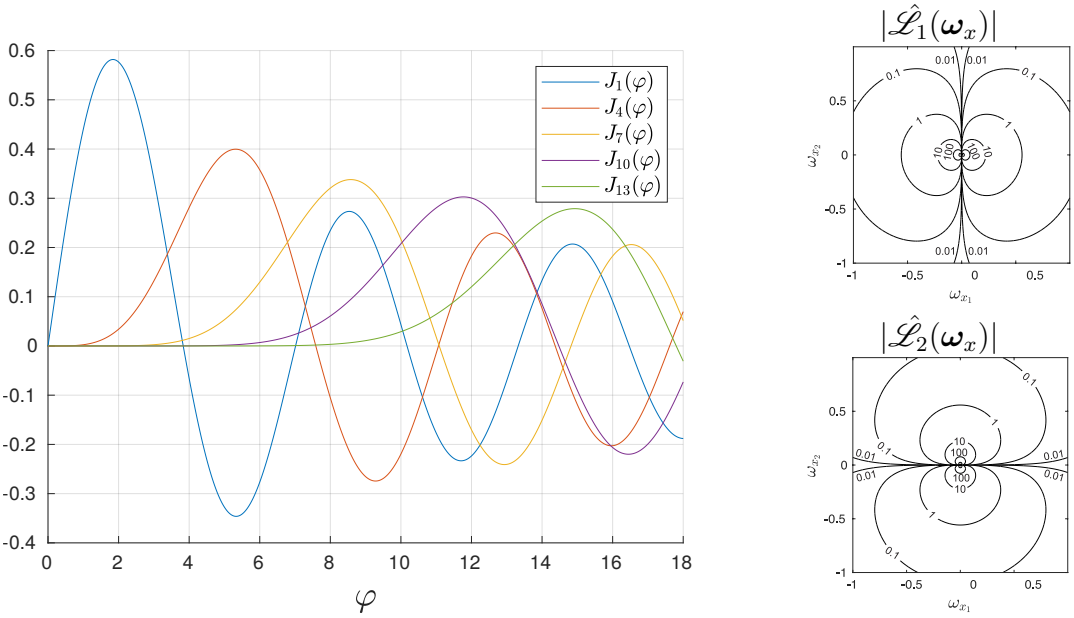

Figure 1. Bessel functions of different order (left) and magnitude of the Fourier transform of the two-dimensional Langevin function in both directions (right). The higher the order of the Bessel function, the greater the distance of its first maximum from the origin.

of the first maximum which also is a global maximum is proportional to its order. This means for the tensor product of the Bessel functions $J_n(x)J_m(y)$ that the global maximum, which simultaneously lies closest to the origin, is located around the position (n, m). The larger n and m, the further away from the origin this maximum lies. The consequence of this is that it is more suppressed by the exponentially decreasing Fourier transformed Langevin function. It follows for the series in (6) and (9) that only summands for which $(n_k, m_k) = (k - \lambda N_B, k - \lambda(N_B - 1))$ is sufficiently close to the origin can contribute significantly. This suggests that the summands for which $n_k^2 + m_k^2$ is minimal have the greatest contribution. The computation of the energy of the individual summands is shown in Fig. 2 and supports this assumption. For clarity, the energy has been computed component-wise by numerical evaluation of (9) over the equidistant grid $\{\omega_{x_{1,0}}, ..., \omega_{x_{1,N_E}}\} \times \{\omega_{x_{2,0}}, ..., \omega_{x_{2,M_E}}\}$ with spacing Δ via

$$\sum_{i=0}^{N_E} \sum_{j=0}^{M_E} |\Delta^2 \hat{\boldsymbol{s}}_k(\omega_{x_{1,i}}, \omega_{x_{2,j}})|^2. \tag{11}$$

Since the orders of the Bessel functions are $-k + \lambda N_B$ and $k - \lambda(N_B - 1)$, the index

$$\lambda_k^* = \arg\min_{\lambda \in \mathbb{Z}} \rho_k(\lambda) = \arg\min_{\lambda \in \mathbb{Z}} (k - \lambda N_B)^2 + (k - \lambda(N_B - 1))^2 \tag{12}$$

contributes the most to the series. The solution of the minimization problem for $\lambda \in \mathbb{R}$ would be given by $\lambda_k^* = (2N_B - 1)k/(2N_B^2 - 2N_B + 1)$, but since λ_k^* must be an integer

and the function $\rho_k(\lambda)$ is a parabola, the solution becomes

$$\lambda_k^* = \text{round}\left(\frac{(2N_B-1)k}{(2N_B^2-2N_B+1)}\right). \tag{13}$$

For a more compact formulation, we are defining the corresponding orders of the Bessel functions

$$\begin{aligned} n_k^* &= -k + \lambda_k^* N_B \\ m_k^* &= k - \lambda_k^*(N_B-1). \end{aligned} \tag{14}$$

The oscillation of the energy of the different frequency components seems to be originated in the rounding of the optimal integer solution λ_k^*. This can also be observed in Fig. 2. The global decay is due to the increasing distance from the origin for increasing frequency component, and the oscillation comes from the rounding. The corresponding orders are also shown in this figure.

It can therefore be seen that the summand determined here makes the largest contribution to the series. In some rare cases, further contributions may be equally large, but not larger. In contrast to the estimation of the optimal summand in [21], where the minimal mixing order which is $\min_{\lambda\in\mathbb{Z}} |k-\lambda N_B| + |k-\lambda(N_B-1)|$ was determined, the index calculated here is still correct for larger frequency components. Furthermore, it can be observed that in those cases in which the contribution of the largest neighboring summand is similar to the assumed summand λ^*, the total energy is generally low compared to the other frequency components. If several summands have a similar contribution for a fixed frequency component k, this implies that the global maxima of the associated Bessel functions have similar distances to the origin. But due to the interrelationship of the orders $(k-\lambda N_B, k-\lambda(N_B-1))$, none of them can be particularly close to the origin for sufficiently large values of N_B. Therefore, the total energy of such a frequency component would be low. Accordingly, the temporal Fourier transformed system function for frequency components with high energy can be approximated by

$$\begin{aligned} \boldsymbol{s}_k(\boldsymbol{x}) \approx & \operatorname{sgn}(\det(\boldsymbol{AG}))\boldsymbol{C}_k(-\mathrm{i})^{\lambda_k^*} \int_{\mathbb{R}^2} \left[\frac{\partial^2}{\partial z_1 \partial z_2}\boldsymbol{\mathscr{L}}(\beta \boldsymbol{G}\boldsymbol{z})\right]_{\boldsymbol{z}=\boldsymbol{x}-\boldsymbol{u}} \\ & V_{n_k^*}\left(\frac{G_x}{A_x}u_1\right) V_{m_k^*}\left(\frac{G_y}{A_y}u_2\right) \mathrm{d}\boldsymbol{u}. \end{aligned} \tag{15}$$

The frequency components for which this approximation is valid are those which are relevant for the reconstruction. Let $\boldsymbol{\mathscr{L}}_{z_1,z_2}(\boldsymbol{y}) = \left[\frac{\partial^2}{\partial z_1 \partial z_2}\boldsymbol{\mathscr{L}}(\boldsymbol{z})\right]_{\boldsymbol{z}=\boldsymbol{y}}$ denote the partial derivative of the Langevin function. Using the substitutions $y_1 = \frac{G_x}{A_x}u_1$ and $y_2 = \frac{G_y}{A_y}u_2$ and the chain rule

$$\left[\frac{\partial^2}{\partial z_1 \partial z_2}\boldsymbol{\mathscr{L}}(\beta \boldsymbol{G}\boldsymbol{z})\right]_{\boldsymbol{z}=\boldsymbol{y}} = \beta^2 \det(\boldsymbol{G})\boldsymbol{\mathscr{L}}_{z_1,z_2}(\beta \boldsymbol{G}\boldsymbol{y}), \tag{16}$$

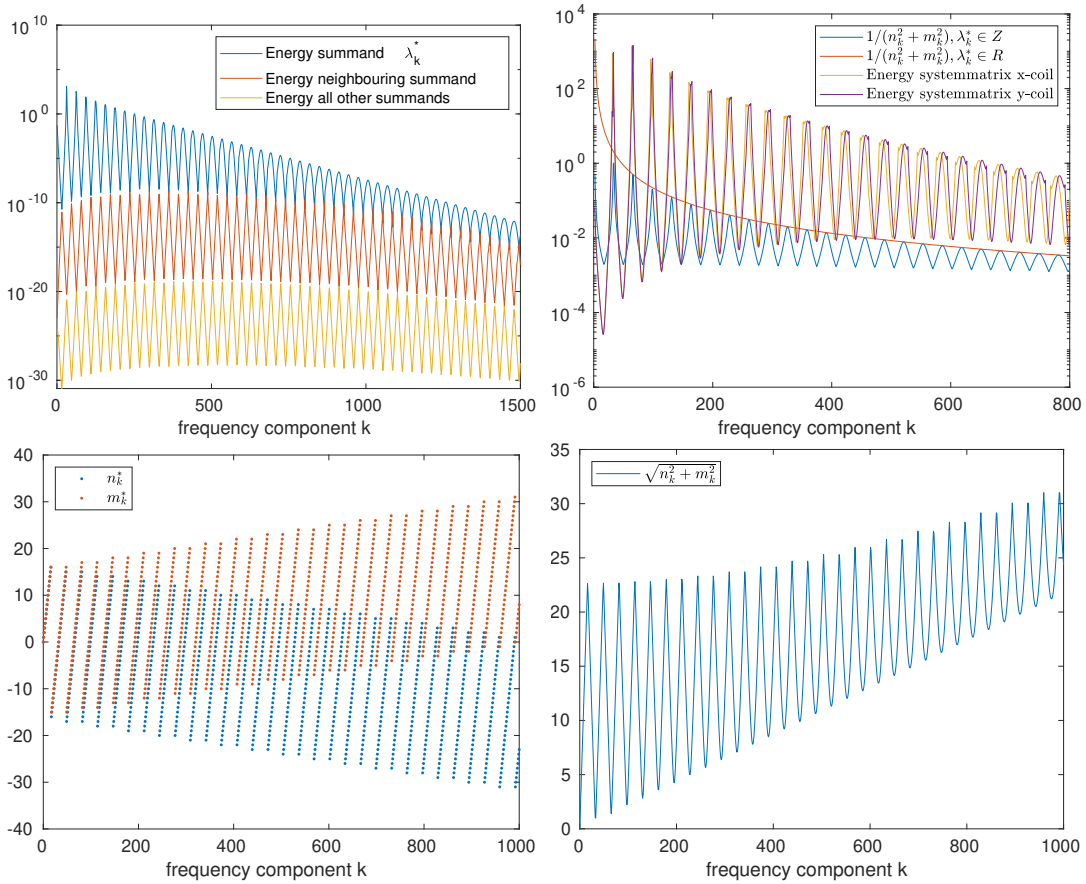

Figure 2. Top left: Energy of the summand associated with λ_k^* and the other summands of the x-coil for $N_B = 33$. The y-coil, i.e., the second component, behaves similar. Top right: Energy of simulated system matrix row and the inverse minimal distance dependent on the frequency component. The wave-like pattern of the energy is originated in the rounding of the optimal index λ. Bottom left: Corresponding orders n_k^*, m_k^* of the Bessel functions that contribute the most to the series in (9) for $N_B = 33$. Bottom right: The distance of the origin to the point (n_k^*, m_k^*) that indicates the position of the global maximum of $J_{n_k^*}(\omega_{x_1}) J_{m_k^*}(\omega_{x_2})$ for $N_B = 33$.

one gets

$$\begin{aligned} \boldsymbol{s}_k(\boldsymbol{x}) \approx & \det(\boldsymbol{A}\boldsymbol{G}^{-1}) \boldsymbol{C}_k (-\mathrm{i})^{\lambda_k^*} \int_{\mathbb{R}^2} \left[\frac{\partial^2}{\partial z_1 \partial z_2} \mathscr{L}(\beta \boldsymbol{G}\boldsymbol{z}) \right]_{\boldsymbol{z}=\boldsymbol{x}-\boldsymbol{G}^{-1}\boldsymbol{A}\boldsymbol{y}} \\ & V_{n_k^*}(y_1)\, V_{m_k^*}(y_2)\, \mathrm{d}\boldsymbol{y} \\ = & \det(\boldsymbol{A}) \beta^2 \boldsymbol{C}_k (-\mathrm{i})^{\lambda_k^*} \int_{\mathbb{R}^2} \mathscr{L}_{z_1,z_2}(\beta \boldsymbol{G}\boldsymbol{x} - \beta \boldsymbol{A}\boldsymbol{y}) \\ & V_{n_k^*}(y_1)\, V_{m_k^*}(y_2)\, \mathrm{d}\boldsymbol{y}. \end{aligned} \tag{17}$$

Note that the vanishing sgn-function in (15) is due to the substitution and the associated changed limits of the integral. This step means for the representation of the temporal

Fourier transformed measured voltage signal that

$$\begin{aligned}\boldsymbol{u}_k &= \int_{\mathbb{R}^2} \boldsymbol{s}_k(\boldsymbol{x}) c(\boldsymbol{x}) \,\mathrm{d}\boldsymbol{x} \\ &\approx \det(\boldsymbol{A}) \beta^2 \boldsymbol{C}_k (-\mathrm{i})^{\lambda_k^*} \int_{\mathbb{R}^2} \int_{\mathbb{R}^2} \boldsymbol{\mathscr{L}}_{z_1,z_2}(\beta \boldsymbol{G}\boldsymbol{x} - \beta \boldsymbol{A}\boldsymbol{y}) \\ &\quad V_{n_k^*}(y_1)\, V_{m_k^*}(y_2)\, \mathrm{d}\boldsymbol{y}\; c(\boldsymbol{x})\,\mathrm{d}\boldsymbol{x}. \end{aligned} \tag{18}$$

Because of Fubini's theorem [22], we can exchange the order of integration, and instead of convolution of the Langevin function with the Chebyshev polynomials we obtain a scaled result of the convolution of the concentration with the scaled partial derivative of the Langevin function, i.e. with

$$\tilde{\boldsymbol{c}}(\boldsymbol{y}) = \left(c(\boldsymbol{z}) * \boldsymbol{\mathscr{L}}_{z_1,z_2}(-\beta \boldsymbol{G}\boldsymbol{z})\right)\left(\boldsymbol{G}^{-1}\boldsymbol{A}\boldsymbol{y}\right) \tag{19}$$

the approximation in (18) can be written as

$$\begin{aligned}\boldsymbol{u}_k \approx & \boldsymbol{C}_k (-\mathrm{i})^{\lambda_k^*} \beta^2 \det(\boldsymbol{A}) \int_{\mathbb{R}^2} V_{-k+\lambda_k^* N_B}(y_1) \\ & V_{k-\lambda_k^*(N_B-1)}(y_2)\, \tilde{\boldsymbol{c}}(\boldsymbol{y})\; \mathrm{d}\boldsymbol{y}. \end{aligned} \tag{20}$$

For clarity, the notation of the convolution in (19) is

$$(a(\boldsymbol{\Phi}\boldsymbol{x}) * b(\boldsymbol{\Psi}\boldsymbol{x}))(\boldsymbol{\Pi}\boldsymbol{y}) = \int_{\mathbb{R}^2} a(\boldsymbol{\Phi}\boldsymbol{x}) b(\boldsymbol{\Psi}(\boldsymbol{\Pi}\boldsymbol{y} - \boldsymbol{x}))\,\mathrm{d}\boldsymbol{x} \tag{21}$$

for two functions $a, b : \mathbb{R}^2 \mapsto \mathbb{R}$ and $\boldsymbol{\Phi}, \boldsymbol{\Psi}, \boldsymbol{\Pi} \in \mathbb{R}^{2\times 2}$. For the multi-dimensional $\boldsymbol{\mathscr{L}}_{z_1,z_2}$, the convolution is performed component-wise.

Chebyshev polynomials of second kind are orthogonal on $[-1, 1]$ with respect to the scalar product weighted with $\sqrt{1-x^2}$ and they form a complete orthogonal set. As a consequence, a function $f \in C^1([-1, 1]^2)$ can be expressed via the series

$$f(x, y) = \sum_{n,m=0}^{\infty} a_{nm} U_n(x) U_m(y). \tag{22}$$

This means for the coefficients a_{nm} that

$$a_{nm} = \frac{4}{\pi^2} \int_{[-1,1]^2} f(x, y) U_n(x) U_m(y) \sqrt{1-x^2}\sqrt{1-y^2}\,\mathrm{d}x\,\mathrm{d}y, \tag{23}$$

i.e., the coefficients have the same form as the frequency components of the measured voltage when leaving out the frequency components k with $-k + \lambda_k^* N_B = 0$ or $k + \lambda_k^*(N_B - 1) = 0$. Defining

$$\mathbb{K} = \{k \in \{0, 1, ..., K\} | n_k^* \neq 0, m_k^* \neq 0\}, \tag{24}$$

with $K \in \mathbb{N}$ the maximal frequency component to be used, the convolved concentration $\tilde{\boldsymbol{c}}$ can be approximated by

$$\tilde{\boldsymbol{c}}(\boldsymbol{x}) \approx \sum_{k \in \mathbb{K}} \frac{4|(k - \lambda_k^* N_B)(k - \lambda_k^*(N_B - 1))|}{\pi^2 \beta^2 \det(\boldsymbol{A})} (\boldsymbol{C}_k)^{-1} \boldsymbol{u}_k \mathrm{i}^{\lambda_k^*} U_{|n_k^*|-1}(x_1) U_{|m_k^*|-1}(x_2). \tag{25}$$

To obtain the concentration c, the result of (25) must be deconvolved and scaled correctly according to (19). Possible methods for the deconvolution are described in Section 2.3.

In total, two approximations were made to obtain (25) that allows for a direct reconstruction. These approximations were first the reduction of the infinite sum in (9) to only one summand which contributes the most to the energy of the series. The second approximation is to exclude frequency components in (25) that do not fullfill the requirements in (24). This is necessary because for these cases there is not a Chebyshev polynomial incoorporated in the signal, see (8). It is not entirely clear what the effect of this deletion of those frequency components will be, but it might lead to errors in the reconstruction process.

It should be noted that, due to the assumptions in (22), $\tilde{c}$ is assumed to have support on $[-1, 1]^2$ only and is thus recovered in this area. After rescaling, this area corresponds to the so-called drive-field FOV (DF-FOV), which is the area covered by the FFP trajectory. However, particles outside the DF-FOV still contribute to the voltage signal because also particles in the vicinity of the FFP change their magnetization. When the FFP is located at the boundary of the DF-FOV, the particles outside still contribute to the measurement. Their influence is less than that of particles inside the DF-FOV though, but in general the assumption of no contribution of such particles is not correct and might lead to additional reconstruction artifacts at the DF-FOV boundaries [23].

2.2. Three-dimensional Lissajous trajectory

The three-dimensional case is similar to the two-dimensional one, but more technical. This is due to the more involved system-function representation in 3D. At first, we need some auxiliary variables to get a compact formulation. These variables are dependent on whether the frequency divider N_B and the frequency component k are even or odd.

Let

$$n(k,\lambda_1,\lambda_2) = \begin{cases} (\lambda_1+2\lambda_2)N_B - k & \text{if } N_B \text{ even}, k \text{ even}, \\ (\lambda_1+2\lambda_2+1)N_B - k & \text{if } N_B \text{ even}, k \text{ odd}, \\ (\lambda_1+\lambda_2)N_B - 2k & \text{if } N_B \text{ odd}, \end{cases}$$

$$m(k,\lambda_1,\lambda_2) = \begin{cases} \frac{k}{2} - (\lambda_1+\lambda_2)(N_B-1) & \text{if } N_B \text{ even}, \\ & \quad k \text{ even}, \\ \frac{k}{2} - (\lambda_1+\lambda_2+\frac{1}{2})(N_B-1) & \text{if } N_B \text{ even}, \\ & \quad k \text{ odd} \\ k - (\lambda_1+\frac{\lambda_2}{2})(N_B-1) & \text{if } N_B \text{ odd}, \end{cases} \tag{26}$$

$$\ell(k,\lambda_2) = \begin{cases} \frac{k}{2} - \lambda_2(N_B+1) & \text{if } N_B \text{ even}, k \text{ even}, \\ \frac{k}{2} - (\lambda_2+\frac{1}{2})(N_B+1) & \text{if } N_B \text{ even}, k \text{ odd}, \\ k - \frac{\lambda_2}{2}(N_B+1) & \text{if } N_B \text{ odd}, \end{cases}$$

and

$$C_k = \frac{-2f_D k\mathrm{i}}{\pi^2}\mu_0 m\boldsymbol{P}. \tag{27}$$

Now the frequency components of the three-dimensional temporal Fourier transformed system function can be written as [17]

$$\begin{aligned} \boldsymbol{s}_k(\boldsymbol{x}) =& C_k \mathrm{sgn}(\det(\boldsymbol{AG})) \sum_{\lambda_1,\lambda_2\in\mathbb{Z}} (-\mathrm{i})^{\lambda_1} \int_{\mathbb{R}^3} \left[\frac{\partial^3}{\partial z_1 \partial z_2 \partial z_3} \mathscr{L}(\beta \boldsymbol{G}\boldsymbol{z})\right]_{\boldsymbol{z}=\boldsymbol{x}-\boldsymbol{u}} \\ & V_{n(k,\lambda_1,\lambda_2)}\left(\frac{G_x}{A_x}u_1\right) V_{m(k,\lambda_1,\lambda_2)}\left(\frac{G_y}{A_y}u_2\right) V_{l(k,\lambda_2)}\left(\frac{G_z}{A_z}u_3\right) \mathrm{d}\boldsymbol{u}. \end{aligned} \tag{28}$$

The spatio-temporal Fourier transform reads [17]

$$\begin{aligned} \hat{\boldsymbol{s}}_k(\boldsymbol{\omega}_x) =& C_k \frac{\pi^3}{|\det(\beta\boldsymbol{G})|} \sum_{\lambda_1,\lambda_2\in\mathbb{Z}} (-1)^{\lambda_1} \hat{\mathscr{L}}\left(\frac{\boldsymbol{G}^{-\mathbf{1}}\boldsymbol{\omega}_x}{\beta}\right) \\ & J_{n(k,\lambda_1,\lambda_2)}\left(\frac{A_x}{G_x}\omega_{x_1}\right) J_{m(k,\lambda_1,\lambda_2)}\left(\frac{A_y}{G_y}\omega_{x_2}\right) J_{l(k,\lambda_2)}\left(\frac{A_z}{G_z}\omega_{x_3}\right). \end{aligned} \tag{29}$$

Since the behavior of the three-dimensional Fourier transformed Langevin function is similar to the one in the two-dimensional case, the same considerations can be applied, e.g. the function

$$\rho_k(\lambda_1,\lambda_2) = n(k,\lambda_1,\lambda_2)^2 + m(k,\lambda_1,\lambda_2)^2 + \ell(k,\lambda_2)^2 \tag{30}$$

must be minimized dependent on λ_1 and λ_2. For N_B odd, the variables n, m and l do not depend on whether the frequency component k is odd or even, so in this case we get the solutions

$$\lambda_{1,k} = \frac{ce_k - 2bd_k}{4ab - c^2} \tag{31}$$

$$\lambda_{2,k} = \frac{cd_k - 2ae_k}{4ab - c^2} \tag{32}$$

for $\lambda_{1,k}, \lambda_{2,k} \in \mathbb{R}$ with the variables

$$\begin{aligned} a &= 2N_B^2 - 2N_B + 1 \\ b &= 1.5N_B^2 + 0.5 \\ c &= 3N_B^2 - 2N_B + 1 \\ d_k &= 2k - 6N_B k \\ e_k &= -6N_B k. \end{aligned}$$

Because the function $\rho_k(\lambda_1, \lambda_2)$ in (30) forms a rotated elliptic paraboloid, the solutions cannot be simply rounded to the nearest integer as in the 2D case to get the optimal integer solution. The easiest way to find the optimal integer solution $\lambda_{1,k}^*$ and $\lambda_{2,k}^*$ of (30) is to compute its value for the four possible combinations of $\lfloor \lambda_{1,k} \rfloor, \lceil \lambda_{1,k} \rceil$ and $\lfloor \lambda_{2,k} \rfloor, \lceil \lambda_{2,k} \rceil$. Here, $\lfloor . \rfloor$ and $\lceil . \rceil$ are denoting the floor and ceiling function, respectively. However, the cases in which the solutions are different from the rounding to the nearest integer are the cases in which the distance is large anyway, so in practice, a simple rounding can be chosen though it is not optimal in all cases. For N_B even, a distinction for k even or odd must be done, but the principle is the same as for N_B odd.

To obtain a more compact formulation later, we introduce the variables

$$\begin{aligned} n_k^* &= n(k, \lambda_{1,k}^*, \lambda_{2,k}^*) \\ m_k^* &= m(k, \lambda_{1,k}^*, \lambda_{2,k}^*) \\ \ell_k^* &= \ell(k, \lambda_{2,k}^*). \end{aligned} \tag{33}$$

The behavior of the energy distribution is similar to that in the two-dimensional case. Here, one summand is sufficient to describe a large part of the energy as well. If several terms are necessary, the total energy of the frequency component is also low.

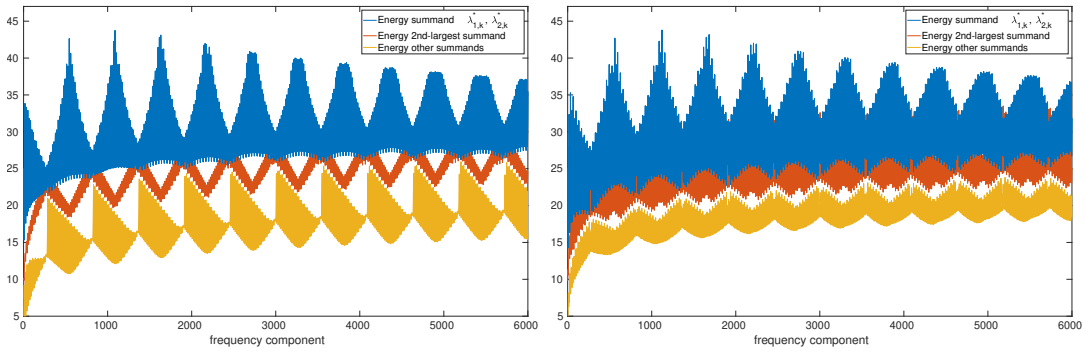

Figure 3. Energy of the summand associated with $\lambda_{1,k}^*, \lambda_{2,k}^*$ and the other summands for the three-dimensional case and $N_B = 33$. Left: x-coil, i.e., first component. Right: y-coil, i.e. second component. The plot for the z-coil looks very similar to the y-coil. It is visible that for very few components with high frequency and low total energy the computed $\lambda_{1,k}^*, \lambda_{2,k}^*$ are not the optimal solution, as another summand has a larger energy. This is possible because the approximation of $\mathscr{L}_{z_1,z_2,z_3}$ as a radially decreasing function is not true close to the axes.

This can also be seen in Fig. 3. In this example, the energy distribution of the summands in the x-coil is better than for the y- and z-coil. This might be due to the frequency dividers of 33 for the x-coil and 32 and 34 for the y- and z-coil, respectively. For certain frequency components, the indices $\lambda_{1,k}^*, \lambda_{2,k}^*$ minimizing (30) are not the optimal ones with the largest contribution. This may occur because the assumption of $\boldsymbol{\mathscr{L}}_{z_1,z_2,z_3}$ being a radially declining function is only an approximation and not true close to the axes. But again, this only occurs when the total energy of the frequency component is low.

With the same procedure as in Section 2.1, we thus obtain in a first step

$$\boldsymbol{u}_k \approx C_k(-\mathrm{i})^{\lambda_{1,k}^*}\beta^3 \det(\boldsymbol{A}) \int_{\mathbb{R}^3} V_{n_k^*}(y_1)\, V_{m_k^*}(y_2)\, V_{l_k^*}(y_3)\, \tilde{\boldsymbol{c}}(\boldsymbol{y})\, \mathrm{d}\boldsymbol{y} \tag{34}$$

with

$$\tilde{\boldsymbol{c}}(\boldsymbol{y}) = (c(\boldsymbol{z}) * \boldsymbol{\mathscr{L}}_{z_1,z_2,z_3}(-\beta \boldsymbol{G}\boldsymbol{z}))\left(\boldsymbol{G}^{-1}\boldsymbol{A}\boldsymbol{y}\right), \tag{35}$$

and with

$$\mathbb{K} = \{k \in \{0,1,...,K\} \mid n_k^* \neq 0, m_k^* \neq 0, l_k^* \neq 0\} \tag{36}$$

the reconstruction of the convolved concentration becomes

$$\tilde{\boldsymbol{c}}(\boldsymbol{x}) \approx \sum_{k\in\mathbb{K}} \frac{-8|n_k^* m_k^* \ell_k^*|}{\pi^3\beta^3 \det(\boldsymbol{A})} (\boldsymbol{C}_k)^{-1} \boldsymbol{u}_k \mathrm{i}^{\lambda_{1,k}^*} U_{|n_k^*|-1}(x_1) U_{|m_k^*|-1}(x_2) U_{|\ell_k^*|-1}(x_3). \tag{37}$$

This still has to be rescaled and deconvolved according to (35) to obtain the final reconstructed particle concentration $c(\boldsymbol{y})$.

2.3. Deconvolution

The results obtained in Sections 2.1 and 2.2 are the SPIO concentrations convolved with the derivative of the Langevin function. Therefore, a deconvolution has to be carried out. There are several methods for doing this. Two methods are presented here. The first one uses knowledge of the kernel, while the second one works without any precise knowledge of the kernel.

2.3.1. Kernel-based deconvolution Assuming the Langevin model, the convolution kernel is the derivative of the Langevin function. For each coil, a reconstruction $\tilde{\boldsymbol{c}}$ is obtained, which is, of course, based on the same ground-truth concentration. Therefore, a system of equations containing the results from the individual coils can be set up, and the solution of this system gives the final SPIO concentration. This can be done in both the temporal frequency range, in which a convolution matrix has to be set up, and the spatio-temporal frequency range, in which the convolution is replaced by a

multiplication. For the deconvolution in spatio-temporal frequency range, let

$$\boldsymbol{L}_i = \begin{pmatrix} \hat{\mathscr{L}}_i(\boldsymbol{\eta}_1) & 0 & \dots & 0 \\ 0 & \hat{\mathscr{L}}_i(\boldsymbol{\eta}_2) & \ddots & \vdots \\ \vdots & \ddots & \ddots & 0 \\ 0 & \dots & 0 & \hat{\mathscr{L}}_i(\boldsymbol{\eta}_N) \end{pmatrix} \tag{38}$$

with $i = 1, ..., d$ denote the transfer matrix for the i-th component where $\boldsymbol{\eta}_j$, $j = 1, 2, \dots, N$ are the discrete spatial frequencies. Then, the regularized minimization problem reads

$$\min_{\boldsymbol{c}\geq 0} \left\| \begin{pmatrix} \boldsymbol{L}_1 \\ \vdots \\ \boldsymbol{L}_d \end{pmatrix} \mathscr{F}(\boldsymbol{c}) - \begin{pmatrix} (\hat{\tilde{c}}_1(\boldsymbol{\eta}_1), \dots, \hat{\tilde{c}}_1(\boldsymbol{\eta}_N))^T \\ \vdots \qquad\qquad \vdots \\ (\hat{\tilde{c}}_d(\boldsymbol{\eta}_1), \dots, \hat{\tilde{c}}_d(\boldsymbol{\eta}_N))^T \end{pmatrix} \right\|_2^2 + \lambda \|\boldsymbol{c}\|_p^p \tag{39}$$

with $\hat{\tilde{c}}_i$ being the spatial discrete Fourier transform of $\tilde{c}_i$ and $\mathscr{F}$ denoting the operator of the discrete Fourier transform. In this case, a regularization with a p-norm, $p \in \mathbb{N}$, has been chosen. Typically p is chosen as $p = 1$ or $p = 2$. When omitting the constraint $c \geq 0$ and choosing $p = 2$ and $\boldsymbol{L} = \left(\boldsymbol{L}_1, \dots, \boldsymbol{L}_d\right)^T$, there is an analytical solution of this minimization problem. It is given by

$$\boldsymbol{c} = \mathscr{F}^{-1} \left(\left(\boldsymbol{L}^H \boldsymbol{L} + \mu \boldsymbol{I}\right)^{-1} \boldsymbol{L}^H \begin{pmatrix} (\hat{\tilde{c}}_1(\boldsymbol{r}_1), \dots, \hat{\tilde{c}}_1(\boldsymbol{r}_N))^T \\ \vdots \qquad\qquad \vdots \\ (\hat{\tilde{c}}_d(\boldsymbol{r}_1), \dots, \hat{\tilde{c}}_d(\boldsymbol{r}_N))^T \end{pmatrix} \right) \tag{40}$$

with the new regularization factor μ that is proportional to λ due to the Plancherel identity and the fact that in (39) the regularization is $\lambda \|\boldsymbol{c}\|_p^p$ and not $\lambda \|\mathscr{F}(\boldsymbol{c})\|_p^p$. Since the $\boldsymbol{L}_i$ are sparse, the calculation of the inverse is possible in an efficient and fast way. For the use of $p = 1$ or other regularization terms, an iterative solver would be necessary, but due to the sparse $\boldsymbol{L}_i$, the solution can still be calculated efficiently. To avoid deconvolution artifacts, it is recommended to use a zero padding of sufficient size when computing the Fourier transforms. To obtain the concentration c, the inverse Fourier transform of the solution has to be computed. In the following, this method is referred to as the SLE deconvolution.

2.3.2. Deconvolution without an explicit kernel If one wants to reconstruct the SPIO concentration without explicit use of the Langevin function as kernel, a deconvolution can also be carried out. On the one hand, this can, of course, be done using methods in which the kernel is estimated - an overview and evaluation of methods can e.g. be found in [24]. Another variant that uses some properties of the Langevin kernel is shown below. The two-dimensional kernel $\boldsymbol{\mathscr{L}}_{z_1,z_2}$ is depicted in Fig. 4 for both directions. It forms approximately the derivative along one dimension, while it is a lowpass filter along the

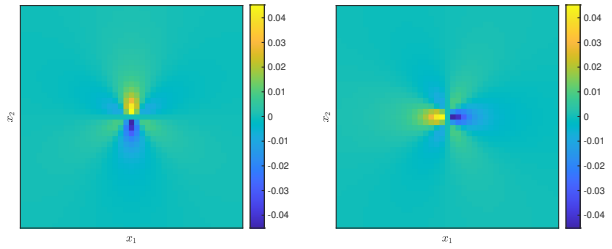

Figure 4. First and second component of $\mathscr{L}_{z_1,z_2}(\boldsymbol{x})$. A convolution with this function corresponds to a highpass filter in one dimension and a lowpass filter in the other dimension.

other dimension. More specifically, the first component of the filter forms the derivative in the x_2-direction and smoothes in the x_1-direction. The second component behaves exactly the other way around: Here, the derivative is formed in the x_1-direction, while smoothing takes place in the x_2-direction. For the three-dimensional case, it forms the derivative in two dimensions, while smoothing the remaining dimension. This is an observation based on the appearance of the derivatives of the Langevin function.

To resolve the derivation, an integration can be applied by summing up $\tilde{c}$ cummulatively in the corresponding dimensions. The result is the blurred SPIO distribution. For a rough representation of the concentration, this step is sufficient and can be calculated very fast. It should be noted that one gets a separate reconstruction for each coil which is blurred in one direction. To combine these different results into a single unblurred reconstruction, the method from [25] can be used which was presented for MPI X-space reconstruction with different resolutions. The proposed method can be easily adapted to the three-dimensional case. A visualization is shown in Fig. 5. In the following, this method is referred to as the Cumsum deconvolution.

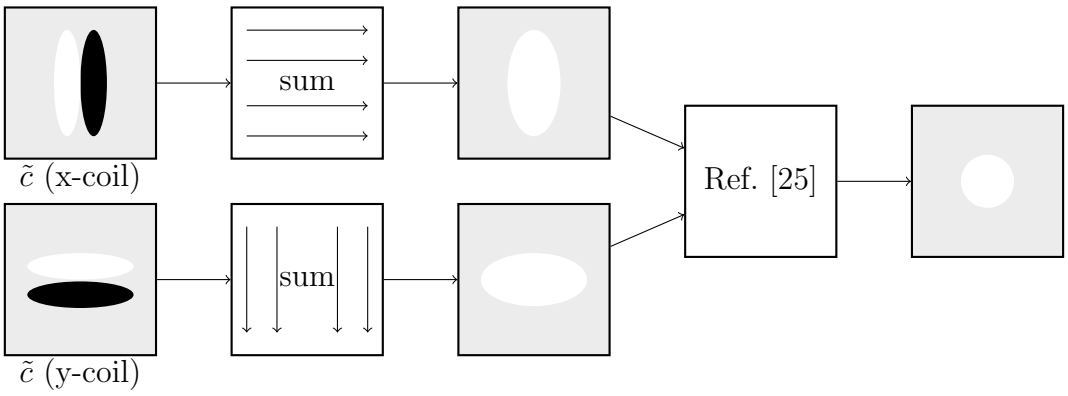

Figure 5. Visualization of the Cumsum deconvolution for the two-dimensional case. The obtained $\tilde{c}$ of each coil, corresponding to the first and second component of $\tilde{c}$, is summed up cummulatively and then merged by using the method of [25].

2.4. Complete approach

Here, a short overview over the steps of the total method is given. For simplicity, it is split up for the two-dimensional and three-dimensional case. The following applies to the former:

1) Map the frequency component k to the orders of the Chebyshev polynomials. For 2D, this is done by computing λ_k^* as in (13). The λ_k^* is used in step 2) to determine the final orders for both directions.
2) Approximate the convolved particle distribution $\tilde{\boldsymbol{c}}$ by applying (25).
3) Rescale and deconvolve the obtained result from Step 2) for recovery of the original particle distribution. The rescaling is done according to (19). Two deconvolution techniques are presented in section 2.3.

The three-dimensional case is similar:

1) Map the frequency component k to the orders of the Chebyshev polynomials. For 3D, this is done by computing $\lambda_{1,k}^*$ and $\lambda_{2,k}^*$. A sufficient approximation is the rounding to the nearest integer value of $\lambda_{1,k}$ and $\lambda_{1,k}$ given in (32). Then the orders $|n_k^*|-1$, $|m_k^*|-1$ and $|\ell_k^*|-1$ of the Chebyshev polynomials in all three dimensions are given by (33).
2) Approximate convolved particle distribution $\tilde{\boldsymbol{c}}$ by applying (37).
3) Rescale and deconvolve the obtained result from Step 2) for recovery of the original particle distribution. The rescaling is done according to (35). The same deconvolution techniques as in 2D can be applied.

2.5. Simulation experiments

To evaluate the proposed method, reconstructions with simulated data with two- and three-dimensional excitation resulting in a Lissajous trajectory were carried out. To deconvolve the obtained $\tilde{\boldsymbol{c}}$, the Cumsum deconvolution and the SLE deconvolution with both ℓ_1 and ℓ_2 regularization were performed. The fast iterative shrinkage thersholding algorithm [26] also known as FISTA was used to solve the ℓ_1-deconvolution problem. To compare the methods the mean absolute error (MAE) is computed. The MAE for two images $A_1, A_2 \in \mathbb{R}^{n_1 \times n_2}$ is

$$\mathrm{MAE}(A,B) = \frac{1}{n_1 n_2} \sum_{i,j=1}^{n_1,n_2} |A_1(i,j) - A_2(i,j)| \,. \tag{41}$$

Since the scaling of the reconstruction using the Cumsum deconvolution is not known due to the unknown kernel and its scaling, all final images were normalized to the range $[0,1]$ to allow for a fair comparison. The parameters from Table 1 were used for the simulations.

The phantoms for two- and three-dimensional simulation are shown in Fig. 6. The 3D phantom is presented as both an isosurface and a slice at $z = 13$ of the x-y-plane

Table 1. Parameters used for obtaining the simulated voltage signal for the experimental simulation part.

Parameter	Value
Particle core diameter	30 nm
Temperature	293 K
Gradient strength 2D	$G_x = G_y = 1\frac{T}{\mu_0 m}$
Excitation amplitudes 2D	$A_x = A_y = 0.0125\frac{T}{\mu_0}$
Excitation frequencies	$(f_x, f_y) = (\frac{2.5}{96}, \frac{2.5}{93}) \cdot 10^6\,\mathrm{Hz}$
FOV 2D	12.5 mm $\times$12.5 mm
Gradient strength 3D	$G_x = G_y = -\frac{1}{2}G_z = 1\frac{T}{\mu_0 m}$
Excitation amplitudes 3D	$A_x = A_y = A_z = 0.0125\frac{T}{\mu_0}$
Excitation frequencies	$(f_x, f_y, f_z) = (\frac{2.5}{93}, \frac{2.5}{96}, \frac{2.5}{99}) \cdot 10^6\,\mathrm{Hz}$
FOV 3D	12.5 mm $\times$12.5 mm $\times$6.25 mm

which includes all six concentration elements of the phantom. Each phantom contains circular or rectangular forms with different concentration and size. A grid of 61×61 pixels in 2D and $41 \times 41 \times 41$ voxels in 3D was used to simulate the voltage vector. The voxel resolution of the reconstruction is freely selectable in each case - here a resolution of 51×51 pixels was used for 2D and a resolution of $31 \times 31 \times 31$ voxels in 3D.

To evaluate the impact of noise, also simulations with added noise has been performed. To this end, the simulated voltage signal has been corruped by Gaussian noise ending up in an SNR of 15 dB, 25 dB and 35 dB. For reconstruction of the corrupted signals, a frequency selection has been made to exclude frequency components with expected poor SNR. The same method explained later in section 2.6 has been used, i.e., the thresholding $(k - \lambda_k^* N_B)^2 + (k - \lambda_k^*(N_B - 1))^2 < \tau$ was tested for each frequency component k. The thresholds $\tau = 120, 220, ..., 820$ were tested. Besides, the regularization parameter λ was optimized in each case for the deconvolution via

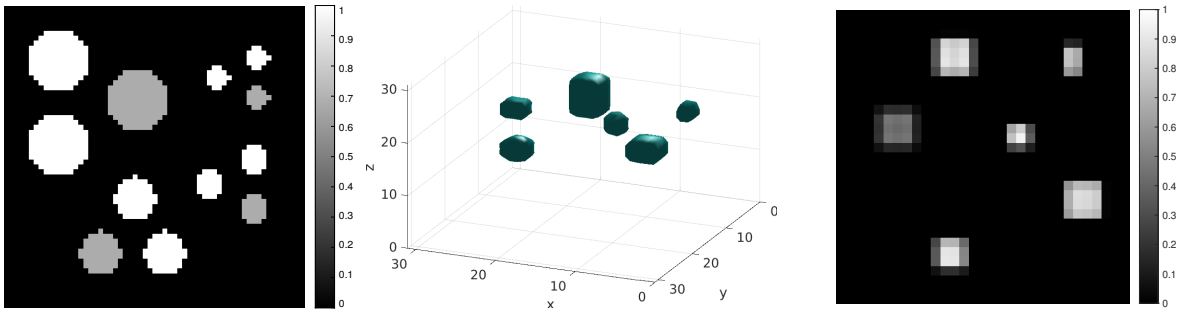

Figure 6. Phantoms for the simulation experiments. Left: two-dimensional phantom. Middle: three-dimensional phantom as an isosurface. Right: Slice of three-dimensional phantom of the x-y-plane at $z = 13$.

SLE-ℓ_2 and SLE-ℓ_1.

2.6. OpenMPIData experiments

To evaluate the direct reconstruction approach on real data, the measurements from the OpenMPIData were used. Neither the reconstruction with a modeled system matrix according to the equilibrium model nor the proposed approach assuming the same equilibrium model worked well on the measured 3D data. Therefore, only the procedure for the 2D data is described in the following. For background correction, the available empty measurements were averaged and then subtracted from the measured system matrix and the measured voltage signal induced by the phantom. Because many steps of the imaging chain in MPI are not covered by the simplified model, like the effects of the analog band-stop filter and a pre-amplifier, the Fourier components of the system function after filtering can be described by (6) and (28), multiplied with $\hat{a}_k$, a complex valued transfer function of the receive chain. The transfer function has to be estimated to reconstruct the measured data. This was done as in [15] by simulation of the system matrix and using a sampling of 3.6% of the measured 2D system matrix. For the sampling, each 3rd pixel in both dimensions of the 2D system matrix inside the DF-FOV was chosen. With this procedure, the transfer function dependent on the frequency components was approximated and then used to adjust the measured voltage signal in Fourier space. With $\hat{a}_{\ell,k}$ being the estimated transfer function for coil ℓ and frequency component k, the corrected frequency components of the voltage signal were calculated as $\tilde{u}_{\ell,k} = \frac{u_{\ell,k}}{\hat{a}_{\ell,k}+\epsilon}$ with the regularization $\epsilon = 10^{-16}$.

It is a standard procedure to exclude frequency components with a low SNR from the reconstruction. Typically, the SNR is estimated based on the measured system matrix. In order to circumvent the use of a measured system matrix, here for the frequency selection a threshold decision was made based on the distance of the orders of the Bessel functions to the origin, i.e. $(k - \lambda_k^* N_B)^2 + (k - \lambda_k^*(N_B - 1))^2 < \tau$ was

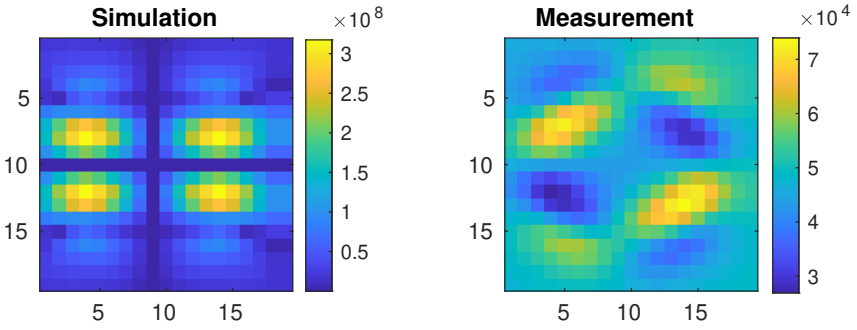

Figure 7. Example for differences of simulated and measured system matrices. The magnitudes of the 3D system matrices of the slice $z = 11$ and frequency component $k = 1551$ are shown. A different shape of the wave hills as well as an additional offset of the values are visible. Since the proposed reconstruction relies on the same model as the simulation, those differences can lead to deviations in the reconstruction.

tested. The threshold was chosen as $\tau = 420$. This has the advantage that no system matrix has to be used to estimate the SNR. Instead, it was assumed that the noise level for each frequency component is at a similar level and thus has less influence on high energy frequency components than on low energy ones. Therefore, the SNR is expected to be better for frequency components contributing a high energy impact, which are those with low Bessel function orders. Thus, the lower the threshold τ, the fewer frequency components are taken into account and their SNR should be higher. The chosen value of $\tau = 420$ is a good compromise. A smaller τ resulted in less accurate detail reconstruction, while higher threshold values lead to more artefacts. Difficulties can be caused by high-energy frequency components that differ strongly from the model, but this is also true for standard SNR-estimation based frequency selection. An example is shown in Fig. 7. This effect could be one of the reasons why this approach did not work well for the 3D case.

The shape phantom and the resolution phantom were reconstructed. These are shown in Fig. 8. Because there is no ground-truth data available, a reconstruction with the measured system matrix was performed and the result was used as ground-truth particle distribution. This reconstruction was done using the Kaczmarz algorithm with Tikhonov regularization with 15 iterations and optimized regularization parameter via grid search. To be precise, the Kaczmarz algorithm was used to minimize the problem $\|Sc - u\|_2^2 + \lambda\|c\|_2^2$, where S is the system matrix. For comparison purposes, a reconstruction with the modeled system matrix was generated according to [15]. The Kaczmarz algorithm was performed with 15 iterations as well and the regularization parameter was also optimized. This comparison is chosen because the simulated system matrix relies on the same simplified model of the system function, so the results of the proposed method cannot be expected to be better.

2.7. Time performance

In addition, the computation times of the Kaczmarz reconstruction and the proposed methods are compared. All computations were performed in MATLAB on an Intel Core i7-7700K 4.20 GHz CPU. The computation time for the pre-calculations of the Chebyshev polynomial values on the interval $[-1, 1]$ is not included, because this has to be computed never again and can be reused for every future reconstruction with the same resolution. However, if implemented efficiently, it takes less than a second for standard resolutions.

3. Results

In this section, the results of the experiments are shown. At first, we look at the reconstruction results for the simulation setup. Then the results for the OpenMPIData and the comparison of the time performance are presented.

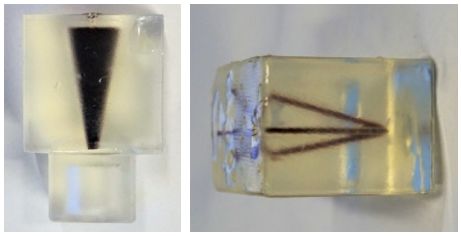

Figure 8. Shape phantom (left) and resolution phantom (right) of the OpenMPIData [19].

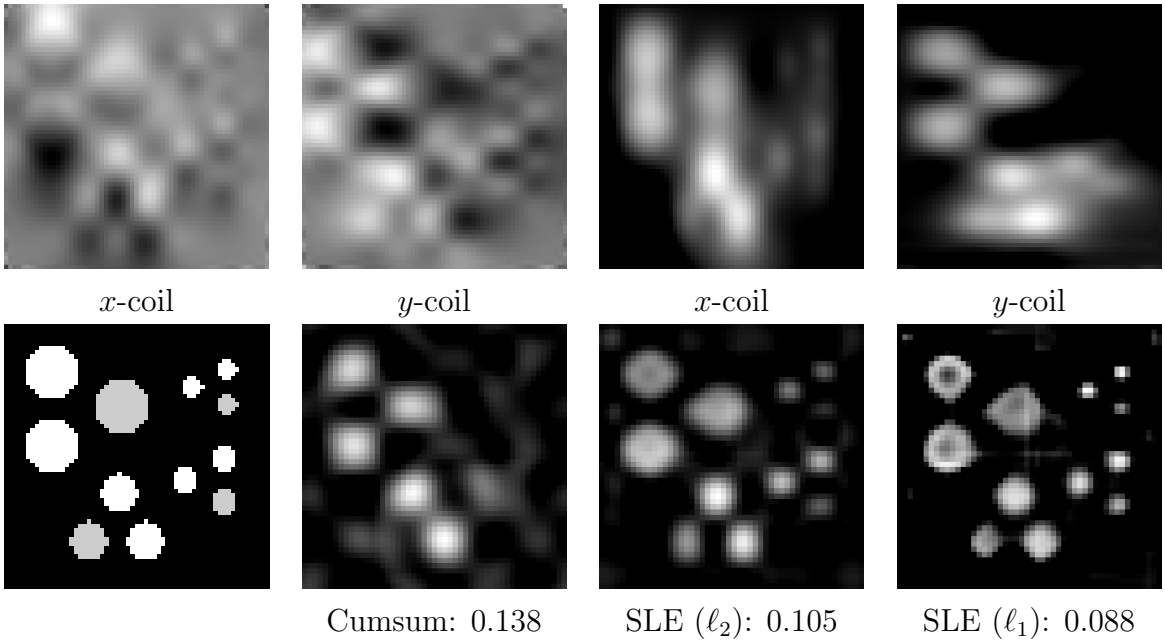

Figure 9. Top: Obtained $\tilde{\boldsymbol{c}}$ (left) and cummulatively summed up $\tilde{\boldsymbol{c}}$ (right) for the x- and y-coil, i.e., the first and second component. Bottom, from left to right: Simulation phantom, deconvolved summed up $\tilde{c}$ and solution of the regularized deconvolution problem with ℓ_2 regularization and ℓ_1 regularization. Below the images the achieved MAE is stated.

3.1. Reconstructions of simulated data

The proposed approach was tested on simulated two- and three-dimensional data. For the two-dimensional simulation setup, the reconstruction of $\tilde{c}$ and the cummulative summation are shown in Fig. 9. One can see the property of the filter mentioned in Section 2.3.2 to form the derivative in one direction. The final reconstructions are also shown in Fig. 9. On the right side the reconstructions using the regularized system of equations with an ℓ_2- and ℓ_1-regularization are depicted, respectively. In both cases the weighting factor λ was chosen to optimize the MAE. The SLE-ℓ_1 deconvolution achieves the best MAE with 0.088 followed by the ℓ_2 regularized with 0.105. The Cumsum deconvolution achieves an MAE of 0.142. The worse MAE of the Cumsum deconvolution image corresponds to the visible blurring in the reconstructed image. Besides, the three

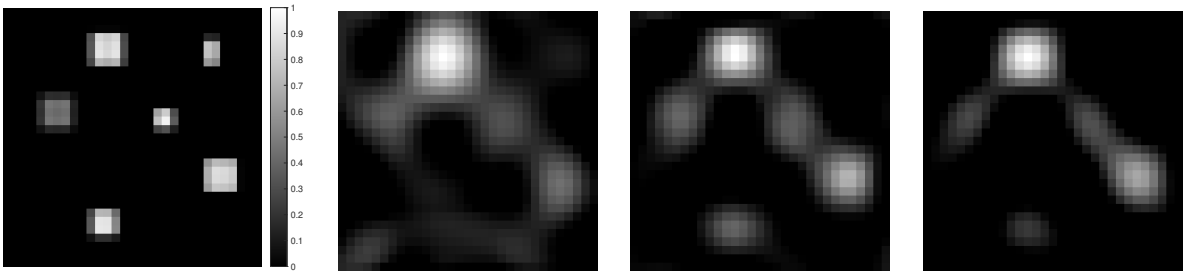

MAE volume:	Cumsum: 0.054	SLE (ℓ_2): 0.033	SLE (ℓ_1): 0.012
MAE slice:	Cumsum: 0.124	SLE (ℓ_2): 0.073	SLE (ℓ_1): 0.060

Figure 10. Reconstruction of the 3D simulation phantom (left) by the proposed approach followed by the Cumsum deconvolution, the SLE deconvolution with ℓ_2 regularization and SLE deconvolution with ℓ_1 regularization (from left to right). To visualize the 3D reconstruction, the x-y-plane at $z = 13$ is shown. The MAE is given for both the total volume as well as for the depicted slice only.

smallest circles are only very weakly indicated. The two other deconvolution techniques are not blurred and resolve the smallest circles. In the ℓ_1 regularized reconstruction some artifacts are visible inside the concentration circles, but it resolves the smaller concentration circles best.

As mentioned before, a three-dimensional reconstruction was performed as well. To visualize the results of the reconstructions, the x-y-plane at $z = 13$ is depicted. The obtained reconstructions are shown in Fig. 10. The smallest concentration element at the border could not be resolved. All other elements are visible when $\tilde{c}$ is deconvolved by the SLE-ℓ_2 or SLE-ℓ_1 deconvolution. The latter one shows less blurring and obtains the best MAE for the presented slice, but resolves some of the elements less clear. The proposed method followed by the Cumsum deconvolution does not resolve the lower element and obtains the worst MAE.

Lastly, the reconstruction results of the simulated signals corrupted by noise are presented. The influence of the thresholding parameter τ and the the obtained images for each tested SNR are shown in Fig. 11. The proposed reconstruction method can cope with noisy data. For an SNR better than 25 dB no thersholding seems to be neccessary, but for the tested SNR of 15 dB the applied thresholding improves the reconstruction quality. The Cumsum deconvolution shows ths most artifacts in the reconstructed images, while the SLE-ℓ_1 deconvolution shows the least artifacts. The SLE-ℓ_2 deconvolution resolves the smaller circles best, but suffers from more artifacts than the SLE-ℓ_1 deconvolution. Nonetheless, it achieves the best MAE for the SNR of 35 dB and only slightly worse MAE values for the other two tested noise levels.

3.2. Reconstructions of OpenMPIData

The reconstruction results for the two-dimensional measurements are depicted in Fig. 12. One can see that the reconstruction with the proposed direct method works on measured

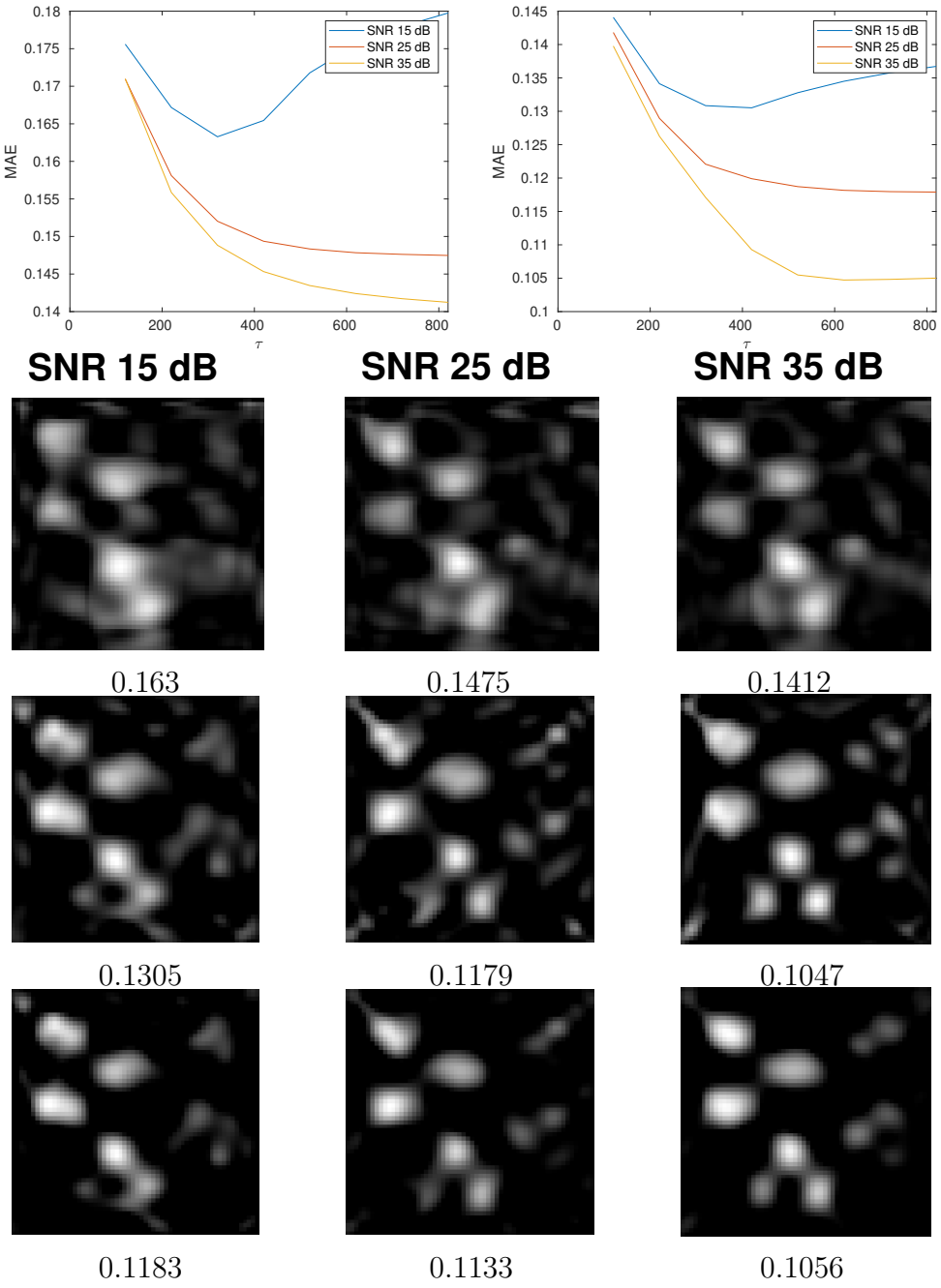

Figure 11. Results of the proposed reconstruction for the 2D simulation phantom with noise corruption. Top: MAE dependent on the rheshold τ for the frequency selection. Results for the reconstruction followed by Cumsum deconvolution (left) and by SLE-ℓ_2 deconvolution (right). The curves of the SLE-ℓ_1 deconvolution behave similar to the SLE-ℓ_2 deconvolution curves. Below: Reconstructed 2D phantoms for an SNR of 15 dB, 25 dB and 35 dB. The achieved MAE is stated below the reconstruction image. The second row shows the reconstruction followed by Cumsum deconvolution, the third row the SLE-ℓ_2 deconvolution and the forth row the SLE-ℓ_1 deconvolution. For each reconstruction image the optimal τ and regularization parameter λ was chosen.

Table 2. Computation time for 2D and 3D setting and different grid sizes of the standard system matrix reconstruction with Kaczmarz algorithm with 5 iterations and the proposed methods.

Reconstruction	Calculation time
Standard, Kaczmarz, grid 51×51	0.074 s
$\tilde{c}$, grid 51×51	0.012 s
- Cumsum deconvolution	0.002 s
- SLE-ℓ_2 deconvolution	0.001 s
- SLE-ℓ_1 deconvolution	0.018 s
Standard, Kaczmarz, grid $31 \times 31 \times 31$	18.735 s
$\tilde{c}$, grid $31 \times 31 \times 31$	0.719 s
- Cumsum deconvolution	0.009 s
- SLE-ℓ_2 deconvolution	0.016 s
- SLE-ℓ_1 deconvolution	0.696 s

two-dimensional data. The shape phantom could be resolved by all three proposed deconvolution techniques. The resolution phantom is fully resolved by the simulated system matrix approach and the proposed approach followed by the SLE deconvolution with an ℓ_1 regularization. Using the two other deconvolution methods, either the outer or the inner structure of the resolution phantom is only weakly indicated. For the proposed method, some artifacts appear at the border of the DF-FOV.

3.3. Time performance

The results of the time measurements for reconstruction are shown in Table 2. It is obvious that the direct reconstruction is significantly faster than the standard Kaczmarz reconstruction. In the 2D setting for the reconstruction of the OpenMPIData, the proposed method followed by the Cumsum deconvolution or SLE-ℓ_2 deconvolution is about five times faster than the state-of-the-art reconstruction using the Kaczmarz algorithm and would allow one to reconstruct more than 70 images per second. With increasing number of pixels the speed advantage increases. The reconstruction of a $31 \times 31 \times 31$ image is about 25 times faster than state-of-the-art Kaczmarz reconstruction, and it takes less than a second using the Cumsum deconvolution or SLE-ℓ_2 deconvolution. Using the SLE-ℓ_1 deconvolution takes longer than the two other methods but is still faster by a factor of 2.5 and 13 for the first and second scenario, respectively.

4. Discussion

The proposed approach can resolve spatial particle concentrations of different sizes for the two- and three-dimensional simulation setup. For this setup, the best MAEs are achieved when the approach is followed by the SLE deconvolution and ℓ_1 regularization.

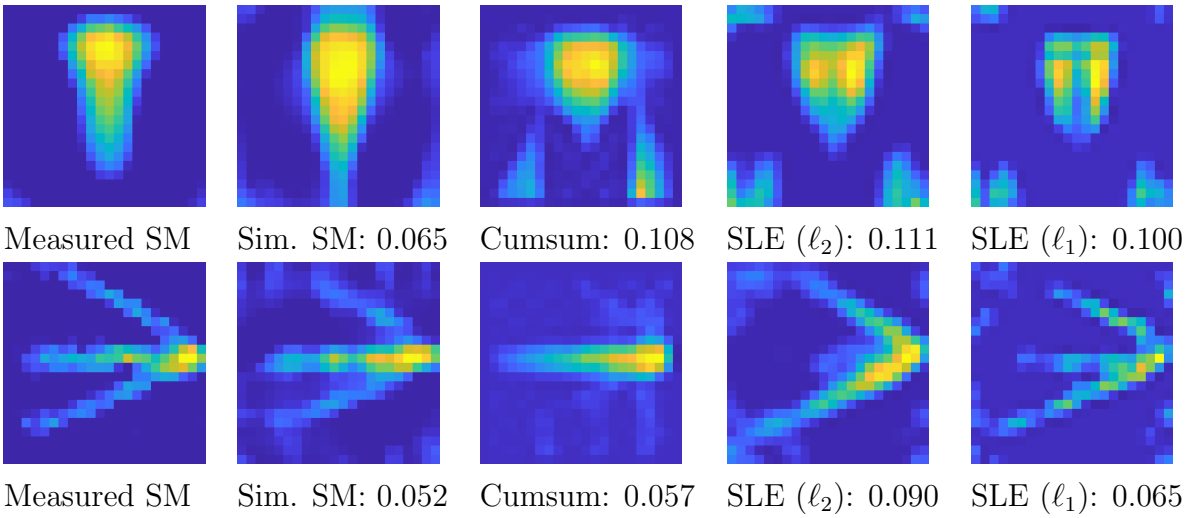

Figure 12. 2D Reconstruction of the OpenMPIData. As the proposed approach only allows for a reconstruction inside the DF-FOV all results are limited to this section. The reconstruction using the measured system matrix (Measured SM) is used as reference to compute the MAE. The value of the MAE of the other reconstruction methods is specified below the reconstruction image. The compared methods are the reconstruction using a simulated system matrix (Sim. SM), the proposed method followed by the Cumsum deconvolution (Cumsum), the proposed method followed by the SLE deconvolution using an ℓ_2 regularization (SLE-ℓ_2) and using an ℓ_1 regularization (SLE-ℓ_1). Top: Reconstructions of the shape phantom. Bottom: Reconstructions of the resolution phantom.

A reconstruction of real data for the two-dimensional setup is also possible. The reconstructions of the real measured data show artifacts, but are comparable to the results of the modeled system matrix reconstruction. Because both methods rely on the same simplified model, the additional artifacts might be caused by the approximations made in the derivation and by SPIOs outside the Lissajous trajectory. Since this method can only reconstruct concentrations within the DF-FOV, values outside the trajectory have a negative influence. Especially the resolution phantom partially sticks out of this area which might lead to artifacts. Besides, for the proposed approach noise has a particular effect at the boundaries of the image because the Chebyshev polynomials have high values (approximately proportional to their order) at these positions. Since there is always noise in the receive chain, this property of the Chebyshev polynomials might lead to fluctuations at the boundaries. However, in this experiment with real data the Cumsum deconvolution technique and the SLE-ℓ_1 deconvolution showed better results, but achieved similar or worse MAE compared to the reconstruction with the simulated system matrix. One should keep in mind that the comparison by means of the MAE referrenced to the reconstruction obtained by using the measured system matrix can only serve as an indicator, as the reference reconstruction itself contains atrifacts and changes dependent on the choice of the regularization term and frequency selection. All presented approaches based on physical models show worse image quality than obtained

by using a measured system matrix. This is not surprising as both methods are based on the same simplified equilibrium model. By estimating a transfer function, some relaxation effects are indirectly incorporated into the model, but effects like the ones seen in Fig. 7 cannot be compensated by the estimated transfer function. Besides, inhomogeneities of the applied magnetic fields and the receive coils lead to further deviations from the model. However, instead of a superior image quality the proposed method is up to several factors faster than the system matrix reconstruction, no matter if measured or simulated. The greater the grid size, the greater the speed advantage. Even with a grid size of $31 \times 31 \times 31$ the image reconstruction needs less than one second while the Kaczmarz reconstruction needs 18 seconds for a single one. Besides, no system matrix has to be stored. Unfortunately, a reconstruction of three-dimensional measured data was not successfull with the proposed approach, while it worked fine on simulated three-dimensional data.

As an adaption, models other than the Langevin model of paramagnetism are possible, as long as the Fourier spectra behave similar, i.e., they are falling with increasing frequency. It seems also possible to incorporate other ratios of the excitation frequencies of the Lissajous trajectory, and to incorporate other trajectories into the model by [17] via replacement of the FFP position function $\boldsymbol{x}_{\mathrm{FFP}}(t)$ in (3).

Due to its fast performance but limited image quality, a possible application could be a fast, rough pre-location of an object to check its position. Of course, some further measurements are still needed to estimate the transfer function, but much less than for obtaining a system matrix - in the experiments 3.6% of the measurements for the system matrix were sufficient for a good estimation of the transfer function. If the transfer function is given, no measurements of the system function are required for reconstruction. This is due to the fact that the orders of the Chebyshev polynomials corresponding to the frequency components and the additional factors are known in advance.

Compared to the proposed direct reconstruction by [16] that compresses a measured system matrix to one coefficient per row, the proposed approach does not need any system matrix because the degrees of the Chebyshev polynomials are known in forehand due to the presented theoretical findings. Instead the estimation of the transfer function is necessary. However, no complete system matrix is needed as this can be estimated with very few individual measurements. Compared to the multi-dimensional direct reconstruction method in X-space by [14], the proposed approach has been shown to be capable of reconstructing real data. Besides, it works in the frequency domain and needs no computationally demanding regridding.

In addition to the proposed reconstruction itself, the derivation of this method provides insights into the mathematical theory of MPI. The observation that the system functions in the case of two- and three-dimensional FFP Lissajous trajectory are similar to tensor products of Chebyshev polynomials of second kind has been described by [7] and [27]. In [21], it was mentioned that only few summands in the infinite series of (6) contribute significantly to the sum in the two-dimensional case. In this work, this

has been extended to the three-dimensional case, and the observations were linked to properties of the Bessel functions and the Fourier transform of the Langevin function. Certain frequency components exist which do not satisfy this regularity. Here it was found that this is true in two cases. First, when multiple summands have a significant impact, i.e. the frequeny component consists of the superposition of several Chebyshev polynomials, and second, when the derived order of the Bessel function does not correspond to a Chebyshev polynomial any more, i.e. the order of the Bessel function is zero.

5. Conclusions and Outlook

For the first time, a direct MPI reconstruction in the frequency domain for two- and three-dimensional Lissajous trajectory excitation was presented which works without a system matrix except for the estimation of the transfer function. The method is based on the Langevin model without relaxation effects. It could be shown that not only simulated data but also real measured two-dimensional data can be reconstructed with this method. The reconstruction is significantly faster than the standard Kaczmarz method and is real-time capable for the presented grid sizes. However, both the simplicity of the underlying model and tracers outside the DF-FOV potentially cause artifacts in the reconstruction, mainly at the boundaries of the DF-FOV.

In a future work it could be investigated whether reconstruction is also possible with Bessel functions as in one-dimensional MPI [18]. A big step to obtain better image quality with this approach would be an extension of the model to include relaxation effects. Simple descriptions of relaxation effects like the Debye relaxation process [28] are already included indirectly by the transfer function, so that more complex models like [10] would be necessary. However, it is questionable whether this is even possible.

References

[1] B Gleich and J Weizenecker. Tomographic imaging using the nonlinear response of magnetic particles. *Nature*, 435(7046):1214–1217, 2005.

[2] P Szwargulski, M Möddel, N Gdaniec, and T Knopp. Efficient joint image reconstruction of multi-patch data reusing a single system matrix in magnetic particle imaging. *IEEE Transactions on Medical Imaging*, 38(4):932–944, 2018.

[3] T Knopp, S Biederer, T Sattel, and T M Buzug. Singular value analysis for Magnetic Particle Imaging. In *2008 IEEE Nuclear Science Symposium Conference Record*, pages 4525–4529. IEEE, 2008.

[4] T März and A Weinmann. Model-Based reconstruction for Magnetic Particle Imaging in 2D and 3D. *Inverse Problems and Imaging*, 10, 05 2016.

[5] T Kluth, B Jin, and G Li. On the degree of ill-posedness of multi-dimensional Magnetic Particle Imaging. *Inverse Problems*, 34(9):095006, 2018.

[6] T Knopp, J Rahmer, TF Sattel, S Biederer, J Weizenecker, B Gleich, J Borgert, and T M Buzug. Weighted iterative reconstruction for Magnetic Particle Imaging. *Physics in Medicine & Biology*, 55(6):1577, 2010.

[7] J Rahmer, J Weizenecker, B Gleich, and J Borgert. Signal encoding in Magnetic Particle Imaging: properties of the system function. *BMC Med Imaging*, 9(4):4, 2009.

[8] J Weizenecker. The Fokker–Planck equation for coupled Brown–Néel-rotation. *Physics in Medicine & Biology*, 63(3):035004, 2018.

[9] T Yoshida and K Enpuku. Nonlinear behavior of magnetic fluid in Brownian relaxation: Numerical simulation and derivation of empirical model. In Thorsten M. Buzug and Jörn Borgert, editors, *Magnetic Particle Imaging*, pages 9–13, Berlin, Heidelberg, 2012. Springer Berlin Heidelberg.

[10] T Kluth, P Szwargulski, and T Knopp. Towards accurate modeling of the multidimensional Magnetic Particle Imaging physics. *New Journal of Physics*, 21(10):103032, 2019.

[11] P W Goodwill and S M Conolly. The X-space formulation of the Magnetic Particle Imaging process: 1-D signal, resolution, bandwidth, SNR, SAR, and magnetostimulation. *IEEE Transactions on Medical Imaging*, 29(11):1851–1859, 2010.

[12] P W Goodwill and S M Conolly. Multidimensional X-space Magnetic Particle Imaging. *IEEE Transactions on Medical Imaging*, 30(9):1581–1590, 2011.

[13] M Grüttner, T Knopp, J Franke, M Heidenreich, J Rahmer, A Halkola, C Kaethner, J Borgert, and T M Buzug. On the formulation of the image reconstruction problem in Magnetic Particle Imaging. *Biomedical Engineering/Biomedizinische Technik*, 58(6):583–591, 2013.

[14] A A Özaslan, A Alacaoglu, O B Demirel, T Çukur, and E U Saritas. Fully automated gridding reconstruction for non-cartesian x-space magnetic particle imaging. *Physics in Medicine & Biology*, 64(16):165018, 2019.

[15] T Knopp, S Biederer, T F Sattel, J Rahmer, J Weizenecker, B Gleich, J Borgert, and T M Buzug. 2D model-based reconstruction for Magnetic Particle Imaging. *Medical Physics*, 37(2):485–491, 2010.

[16] L Schmiester, M Möddel, W Erb, and T Knopp. Direct image reconstruction of Lissajous-type Magnetic Particle Imaging data using Chebyshev-based matrix compression. *IEEE Transactions on Computational Imaging*, 3(4):671–681, 2017.

[17] M Maass and A Mertins. On the Representation of Magnetic Particle Imaging in Fourier Space. *International Journal on Magnetic Particle Imaging*, 6(1):1–21, 2020.

[18] M Maass, C Droigk, and A Mertins. MPI reconstruction using bessel functions. *International Journal on Magnetic Particle Imaging*, 6(2 Suppl 1), 2020.

[19] T Knopp, P Szwargulski, F Griese, and M Gräser. OpenMPIData: An initiative for freely accessible magnetic particle imaging data. *Data in brief*, 28:104971, 2020.

[20] T Knopp and T M Buzug. *Magnetic Particle Imaging: An Introduction to Imaging Principles and Scanner Instrumentation*. Springer, Berlin/Heidelberg, 2012.

[21] M Maass, C Droigk, and A Mertins. A novel representation of the MPI system function. *International Journal on Magnetic Particle Imaging*, 6(2 Suppl 1), 2020.

[22] R L Allen and D Mills. Signal analysis: time, frequency, scale, and structure, 2004.

[23] A Weber, F Werner, J Weizenecker, T M Buzug, and T Knopp. Artifact free reconstruction with the system matrix approach by overscanning the field-free-point trajectory in magnetic particle imaging. *Physics in Medicine & Biology*, 61(2):475, 2015.

[24] A Levin, Y Weiss, Fr Durand, and W T Freeman. Understanding and evaluating blind deconvolution algorithms. In *2009 IEEE Conference on Computer Vision and Pattern Recognition*, pages 1964–1971. IEEE, 2009.

[25] F Werner, N Gdaniec, and T Knopp. Improving the spatial resolution of bidirectional cartesian MPI data using Fourier techniques. *International Journal on Magnetic Particle Imaging*, 3(1), 2017.

[26] A Beck and M Teboulle. A fast iterative shrinkage-thresholding algorithm for linear inverse problems. *SIAM J Imaging Sci*, 2(1):183–202, 2009.

[27] J Rahmer, J Weizenecker, B Gleich, and J Borgert. Analysis of a 3-d system function measured for magnetic particle imaging. *IEEE transactions on medical imaging*, 31(6):1289–1299, 2012.

[28] L R Croft, P W Goodwill, and S M Conolly. Relaxation in X-space Magnetic Particle Imaging.

IEEE transactions on medical imaging, 31(12):2335–2342, 2012.